EARTH SURFACE PROCESSES AND LANDFORMS
Earth Surf. Process. Landforms (2019)
© 2019 John Wiley & Sons, Ltd.
Published online in Wiley Online Library
(wileyonlinelibrary.com) DOI: 10.1002/esp.4613

From Grain to Floodplain: Evaluating heterogeneity of floodplain hydrostatigraphy using sedimentology, geophysics, and remote sensing

H.F. Malenda,[1*†] N.A. Sutfin,[2†] G. Guryan,[3†] S. Stauffer,[2†] J.C. Rowland,[2] K.H. Williams[4,5] and K. Singha[1]
[1] Hydrologic Science and Engineering Program, Colorado School of Mines, Golden, CO
[2] Earth and Environmental Science Division, Los Alamos National Laboratory, Los Alamos, NM
[3] Geology Department, Colorado College, Colorado Springs, CO
[4] Earth and Environmental Sciences Area, Lawrence Berkeley National Laboratory, Berkeley, CA
[5] Rocky Mountain Biological Laboratory, Gothic, CO

Received 30 April 2018; Revised 3 March 2019; Accepted 12 March 2019

*Correspondence to: H.F. Malenda, Hydrologic Science and Engineering Program, Colorado School of Mines, Golden, CO. E-mail: helenmalenda@gmail.com
[†]Affiliation at time of the study

ESPL
Earth Surface Processes and Landforms

ABSTRACT: Stratigraphy is a fundamental component of floodplain heterogeneity and hydraulic conductivity and connectivity of alluvial aquifers, which affect hydrologic processes such as groundwater flow and hyporheic exchange. Watershed-scale hydrological models commonly simplify the sedimentology and stratigraphy of floodplains, neglecting natural floodplain heterogeneity and anisotropy. This study, conducted in the upper reach of the East River in the East River Basin, Colorado, USA, combines point-, meander-, and floodplain-scale data to determine key features of alluvial aquifers important for estimating hydrologic processes. We compare stratigraphy of two meanders with disparate geometries to explore floodplain heterogeneity and connectivity controls on flow and transport. Meander shape, orientation, and internal stratigraphy affected residence time estimates of laterally exchanged hyporheic water. Although the two meanders share a sediment source, vegetation, and climate, their divergent river migration histories resulted in contrasting meander hydrofacies. In turn, the extent and orientation of these elements controlled the effective hydraulic conductivity and, ultimately, estimates of groundwater transport and hyporheic residence times. Additionally, the meanders' orientation relative to the valley gradient impacted the hydraulic gradient across the meanders—a key control of groundwater velocity. Lastly, we combine our field data with remotely sensed data and introduce a potential approach to estimate key hydrostratigraphic packages across floodplains. Prospective applications include contaminant transport studies, hyporheic models, and watershed models. © 2019 John Wiley & Sons, Ltd.

KEYWORDS: Fluvial geomorphology; surface-groundwater exchange; alluvial aquifers; hydrology; geophysics

Introduction

Meandering rivers transport and deposit sediment and in doing so, spatially organize materials, generally into discrete sediment packages, such as point-bar, overbank, and channel-fill deposits. As rivers migrate and change form, they create new sediment deposits and bedforms while abandoning others. Former bedforms provide a structural element to alluvial aquifers, and packages of former floodplain sediment (strata) create natural heterogeneity and anisotropy at the floodplain scale (Figure 1; Allen 1970; Todd 1980; Miall 1996; Van Den Berg & De Vries 2003).

Floodplain strata create spatial variations in hydraulic conductivity, influencing subsurface solute and contaminant fate and transport (e.g. Gelhar & Axness 1983; Dagan 1988; Koltermann & Gorelick 1996; Fogg *et al.* 2000; Heeren *et al.* 2010), surface-groundwater (hyporheic) exchange processes (e.g. Poole *et al.* 2006; Jones *et al.* 2008; Buffington & Tonina 2009; Krause *et al.* 2013), river migration (e.g. Howard, 1992, 1996; Hooke, 2007; Güneralp & Rhoads 2011; Motta *et al.* 2012; Van Dijk *et al.*, 2012, 2013), and connections between the river and surrounding aquifer (e.g. Pringle 2003; Freeman *et al.* 2007; Jencso *et al.* 2009; Argiroff *et al.* 2017). Importantly, stream-aquifer connectivity controls the movement and transport of solutes through the river corridor (e.g. Bencala 1993; Harvey & Fuller 1998; Battin *et al.* 2008; Boehlke *et al.* 2009; Miller *et al.* 2014; Savoy *et al.* 2017), affecting both stream and riparian health (e.g. Findlay 1995; Brunke & Gonser 1997; Boulton *et al.* 1998). The connectivity of hydrofacies—stratigraphic facies with internally consistent hydraulic properties—is an important attribute of geologic heterogeneity within floodplains (Savoy *et al.* 2017). For example, preferential flow paths—connected hydrofacies with high hydraulic conductivity—can increase transport velocities and limit solute sorption processes in alluvial aquifers (e.g. Fuchs *et al.* 2009; Heeren *et al.* 2010; Miller *et al.* 2014). Characterizing the extent,

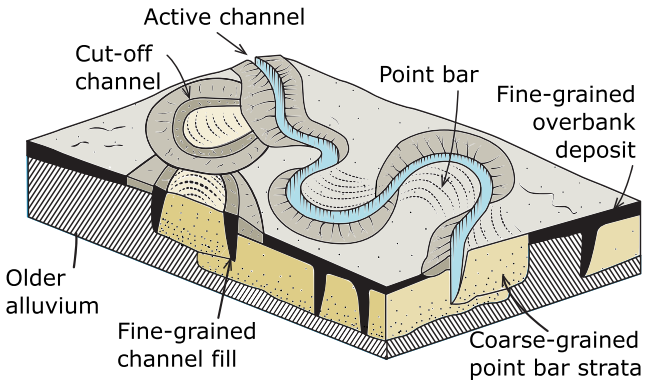

Figure 1. Cartoon depicting river migration, abandonment of former bedforms, and incorporation of fluvial strata into the alluvial aquifer. Modified from Allen (1970). Note variability of homogeneity and heterogeneity within the sediment architecture. [Colour figure can be viewed at wileyonlinelibrary.com]

orientation, and connectivity of floodplain strata is key to evaluating physical and chemical hydrologic processes within river corridors (e.g. Tockner *et al.* 1999; Larsen *et al.* 2012; Stone *et al.* 2017).

Despite the influence of floodplain stratigraphy and hydrofacies connectivity on hydrologic processes in stream-aquifer systems, many hydrologic models simplify floodplain heterogeneity due to difficulties related to hydrogeomorphic field data collection, particularly at ecologically significant scales (i.e. watersheds and river networks; Harvey & Gooseff 2015). For example, hydrologic models at the river-network scale commonly resort to permeability estimates related to median grain sizes to represent alluvial aquifers (e.g. Boano *et al.* 2006; Revelli *et al.* 2008; Kiel & Cardenas 2014; Gomez-Velez *et al.* 2015), reducing floodplains to homogeneous substrates. However, at the channel-scale, heterogeneity of floodplain hydraulic conductivity can facilitate preferential flow paths of hyporheic flow, or can drive surface water exchanged in the floodplain back into the river channel (e.g. Tonina and Buffington, 2007). These mechanisms ultimately shorten the residence time of water in the hyporheic zone (Tonina and Buffington, 2007). If a singular grainsize and homogeneous hydraulic conductivity are used to represent entire reaches of floodplains in hyporheic exchange models, small-scale but frequent exchanges might be overlooked, ultimately underestimating ecologically significant exchanges (e.g. Gomez-Velez & Harvey 2014).

The question remains as to what methods best estimate sediment facies and their connectivity at floodplain scales, and evaluate how that connectivity has evolved through time. For example, ground-penetrating radar (GPR) has been used to map contacts between sediment packages in alluvial systems (e.g. Jol & Smith 1991; Bridge, 2009), but primarily has been used at the field- and meander-scale, due to cost, labor, and time restrictions. To give GPR transects and interpreted fluvial stratigraphy broader geomorphic context, the data can be compared to historical images, maps, or satellite imagery (e.g. Poole *et al.* 2002; Słowik 2016). However, alone these remotely sensed data sources can be both spatially and temporally limited, particularly in inaccessible regions, making it difficult to identify channels abandoned prior to collection of datasets, useful to mapping subsurface pathways.

Current floodplain vegetation and topography can provide a guide to former river locations and associated sediment deposits. Reoccurring disturbance of abandoned channels caused by river reoccupation during flooding, and the gradual nature of vegetative colonization, create contrasting vegetation densities and distributions between former channels and the adjacent floodplain (Poole *et al.* 2002; Greco *et al.* 2007; Egger *et al.*, 2015; Bätz *et al.* 2016). Consequently, vegetation distributions may be used to infer hydrogeomorphic features, such as former channels or gravel bars (Greco *et al.* 2007). Former channels are also generally lower than the adjacent floodplain and can exhibit surface depression and ponded water features, which light detection and ranging (LiDAR; Notebaert *et al.*, 2009; Bertoldi *et al.*, 2011) and Normalized Difference Water Index (NDWI; McFeeters, 1996) can illuminate, respectively. The combination of remote datasets sensitive to vegetation and elevation disparities may enhance our ability to infer hydrogeomorphic features, such as former channels or gravel bars, which may not be obvious from static images, or one remote dataset, alone.

This study explores a framework for mapping 3-D sediment architecture, including the spatial extent of and relations between fluvial deposits, to distill floodplain strata into packages related to current and former channel features. We proffer an approach using geophysics, surficial vegetation and elevation signatures to map hydrostratigraphic facies to increase the portability of stratigraphic field data. The goal of this multiscale study was to present a framework that bridges the divide between detailed, small-scale field studies and the large-scale physical representation of floodplain alluvial aquifers needed in numerical models. We related point-scale sediment core descriptions, estimates of hydraulic conductivity from slug tests, meander-scale GPR transects, and maps of abandoned channels based on remote and historical imagery to infer 3-D river stratigraphy in the East River floodplain. In addition to tracking past river migration using historical photography, we detected additional former channel locations by combining LiDAR, National Agriculture Imagery Program (NAIP) images, and WorldView-2 (WV-2) 8-band multispectral data. We compared observed stratigraphy of two meanders with disparate geometries to estimate floodplain heterogeneity and strata connectivity based on former channel locations and meander geometry. We then considered hydrological impacts of assigning representative sediment characteristics, such as hydraulic conductivity, to inferred hydrofacies.

Study Setting

Upper East River Basin

The East River flows southeast through a subalpine valley near Mount Crested Butte in the West Elk Mountain Range, Colorado, USA. The drainage basin ranges in elevation from 4090 m at the headwaters to 2440 m at the East River's confluence with the Taylor River, forming the Gunnison River. This study focuses on the upper portion of the East River from the headwaters to the confluence with Brush Creek, ~5 km west of Crested Butte, CO, and includes a drainage area of ~134 km^2 (Figure 2).

Surficial deposits that comprise the East River's sediment source vary from rock glaciers, talus, and landslide deposits in the headwaters to lateral moraine deposits flanking lower gradient floodplains downstream. Localized areas of Cretaceous Mancos shale are exposed in-channel and exhibit varying degrees of metamorphism (Gaskill *et al.* 1991). The channel morphology varies greatly along the river's path, alternating between sinuous, unconfined reaches to straighter, more confined sections.

Similar to other Colorado rivers that source former glacial deposits in snowmelt-dominated systems (Andrews 1984; Wohl 2004; Livers & Wohl 2015), the East River floodplain is

© 2019 John Wiley & Sons, Ltd.

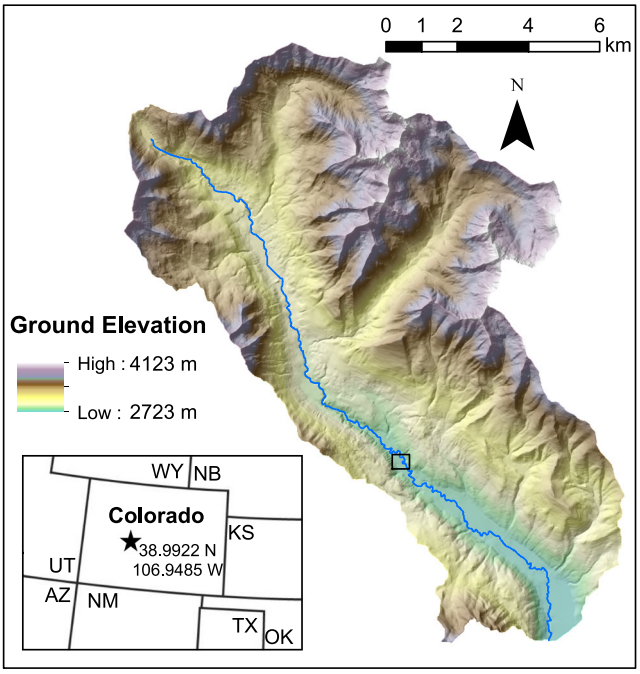

Figure 2. Upper portion of the East River basin and shaded topography. Blue line traces the East River. Black box denotes study area within the basin. [Colour figure can be viewed at wileyonlinelibrary.com]

comprised of heterogeneous sediments, from silts and sands to large gravels and boulders. Additionally, previously glaciated subalpine systems like this one are characterized by shallow down-valley gradients (Wohl, 2004) inherited by alpine glacial processes (Brardinoni and Hassan, 2007; Livers and Wohl, 2015); heterogeneous floodplain sediments sourced from landslides and moraine deposits (Brardinoni and Hassan, 2007; Livers and Wohl, 2015); and channel morphologies that reflect previous climates and sediment supplies (Andrews 1984; Wohl 2004; Livers & Wohl 2015).

The East River is a snowmelt-dominated system, consisting of high flows in late spring and consistently low flows beginning in late summer and continuing through winter and early spring. There is currently no USGS gauge along the upper portion of East River; however, for water year 2015, mean daily flows, measured with a stilling well at the study site, ranged from ~1.0-14.0 m^3/s (Winnick *et al.*, 2017). Downstream, near Almont, the East River achieves bankfull discharge over 20 days per year, during which the majority of bed mobilization occurs (Andrews, 1984).

Detailed Study Area

The study site is near Crested Butte Mountain Resort's pump house (38.99219 N, 106.94854 W), ~8 km downstream of the river's headwaters. Along the study area, the river floodplain is flanked to the northeast and southwest by lateral moraines and small outcrops of Mancos shale exposed along the channel (Figure 3a; Gaskill *et al.* 1991). The southwest valley wall is steep and includes landslide and alluvial-fan deposits (Gaskill *et al.*, 1991). The valley width along the field site is ~150 m, and the average bankfull width is 15 m.

Piezometer networks, sediment descriptions, water level data, and GPR surveys focused on two meanders along an actively migrating portion of the East River, herein referred to as "Meander A" and "Meander D", and additional GPR data were collected near a channel chute cutoff that formed ~10 years ago (herein referred to as the 2007 cutoff, Figure 3c). Piezometer networks consisted of four and five piezometers at Meander A and Meander D, respectively, which provided groundwater elevations and information on sediment type. We co-located GPR transects with piezometers for subsurface control on strata and water table elevations. We conducted two additional GPR surveys near the 2007 cutoff, but there are no piezometers at this location.

We chose Meanders A and D for their contrasting geometries and orientations to the valley, as well as their locations respectively upstream and downstream of the 2007 cutoff. Meander A is more sinuous and bilaterally symmetrical than Meander D (Figure 3b and 3c). Both meanders' active channels contain heterogeneous bed sediments, but meander A's range from silt- to cobble-sized while Meander D's span from silt- to boulder-sized. Graminoids, forbes, and willows (*Salix sp.)* dominate floodplain vegetation (Harte & Shaw 1995). The average water slope of both locations is 0.003, as measured in late summer 2016 by both a field survey using a high precision Trimble GPS unit and from a digital elevation map created from a drone survey (Pai *et al.*, 2017).

A key difference between the two meanders is their position within the context of the floodplain's other geomorphic features, which can affect the hydrologic conditions, and ultimately meander migration. Meander A, and the two meanders immediately downstream of Meander A, are oriented cross-valley, while Meander D is oriented down-valley (Figure 3a). Although both meanders are immediately downstream of relatively straight reaches, Meander A is located downstream of a straight channel that is eroding valley wall material and is immediately upstream from an alluvial-fan deposit. Meander D is located directly downstream of the 2007 cutoff, and up-valley of a meandering reach (Figure 3a). Flooding of the 2007 cutoff still occurs during peak discharge, and late summer monsoons can create depression storage in this low-lying feature. Both the meanders' orientations relative to the valley gradient, as well as their location relative to stable and unstable conditions, affect local hydrologic conditions, sediment supply, and therefore meander evolution.

Methods

Piezometer Installation and Sediment Descriptions

We installed piezometer networks in Meander A and Meander D in July 2016 and July 2015, respectively, by hand auger and backpack drill combined; both drill bits were approximately 6.4 cm in diameter. We measured ground-surface elevations at each piezometer using high-precision Trimble GPS units and a Topcon GPT-8200A auto-tracking pulse total station and Real Time Kinetic GPS. We recovered sediment cores using the auger, and sediment textures were described using standard National Resources Conservation Service (NRCS) soil texture classification methods (Thein, 1979). Piezometer casing consisted of 5.08 cm inside-diameter, 6.03 cm outside-diameter PVC and had screens of 2-mm slotted PVC. Screened intervals ranged in length between 35 and 76 cm, placed at the base of the wells (Table I). We developed the piezometers by flushing and pumping, and added sand packs as needed; gaps between the well casing and borehole were small (<0.5 cm).

GPR Data Acquisition and Processing

GPR is a well-established geophysical method used to map contacts between disparate sediment packages in alluvial systems (e.g. Jol & Smith 1991; Bridge, 2009). The method is based on differences in electromagnetic impedance of surveyed materials (or in non-magnetic materials, the dielectric

© 2019 John Wiley & Sons, Ltd.

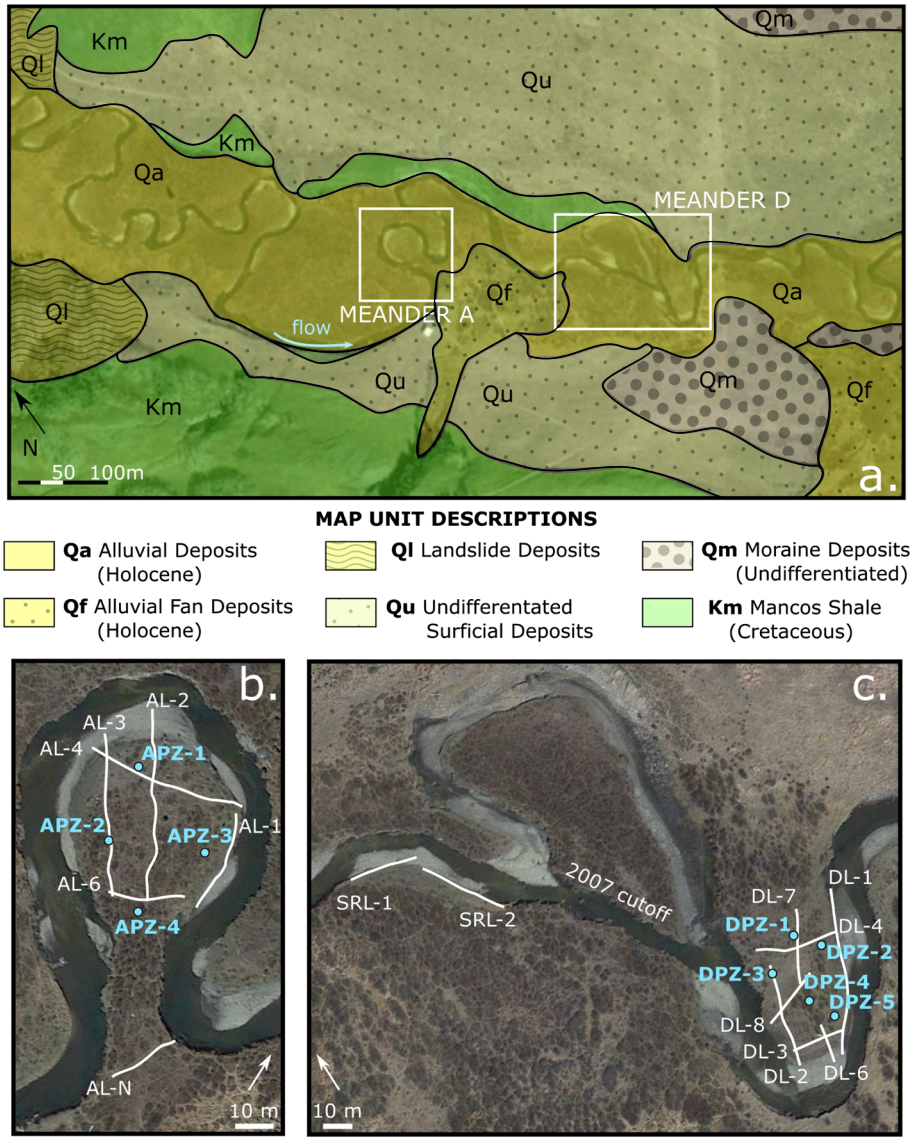

Figure 3. Study area with surficial geology. a) Site with overlay of geology. Geology modified from Gaskill et al. (1991). Flow direction is from left to right. b) Locations of GPR transects (white lines) and piezometers (blue dots) at Meander A. c) Locations of GPR transects and piezometers near Meander D and the recent cutoff. "A", "D", and "SR" denote Meander A, Meander D, and straight reach, respectively. "PZ" indicates piezometer, and "L" indicates a GPR line. Sediment core descriptions and slug test data are associated with each piezometer. [Colour figure can be viewed at wileyonlinelibrary.com]

Table I. Piezometer details for networks at Meanders A and D (Figures 3b, 3c). Location is in Universal Transverse Mercator (UTM, Zone 13 N), ground elevation is in meters above mean sea level, the depth of the well is the depth below ground surface, and the screen length is in meters

Piezometer Name	UTM-N [m]	UTM-E [m]	Ground Elevation [m]	Depth [m]	Screen Length [m]
APZ-1	4309873.23	330920.2301	2774.343	0.62	0.475
APZ-2	4309852.056	330922.5466	2774.153	0.43	0.35
APZ-3	4309861.628	330945.7063	2773.969	1.06	0.762
APZ-4	4309830.465	330941.6139	2774.307	0.80	0.7
DPZ-1	4309847.459	331196.257	2756.746	0.90	0.762
DPZ-2	4310060.674	330990.808	2756.381	0.60	0.762
DPZ-3	4309843.797	331185.165	2756.81	0.85	0.762
DPZ-4	4309827.884	331193.337	2756.61	1.25	0.762
DPZ-5	4309818.749	331198.819	2756.416	1.00	0.762

permittivity) due to changes in moisture or contacts between different sediment compositions (Bridge 2009; Annan 2009). Radar facies—patterns of GPR-reflection characteristics of specific subsurface features—have been used in fluvial environments to interpret fluvial stratigraphy and subsurface sediment architecture (e.g. Vandenberghe & Van Overmeeren 1999; Ekes & Hickin 2001; Skelly *et al.* 2003; Kostic & Aigner 2007; Słowik, 2016). We used GPR to image the distribution and connectivity of floodplain sediments at the two meanders of interest (Lines AL-1 through 6 in Meander A and DL-1 through 7 in Meander D), as well as near the 2007 cutoff (Lines SR-1 and SR-2; Figure 3c). We strategically co-located GPR transect

© 2019 John Wiley & Sons, Ltd.

grids with shallow piezometers at Meanders A and D (Figure 3b and 3c, respectively), where we used water table depths and sediment core descriptions at each piezometer for subsurface control. We also positioned the GPR transects near a current point-bar and the 2007 cutoff to capture radar facies of known features within the floodplain. We recorded all GPR transects with a PulseEKKO™ Pro system by Sensors & Software Inc. using 100 MHz antennae (Davis & Annan 1989). Imaging depth of the GPR was less than 3 m, due to signal attenuation caused by silt and clay content of subsurface and shallow water table. The transmitter and receiver were attached to a sled at a fixed separation of 0.50 m and dragged slowly across each transect. We collected common-offset measurements with a spacing of 0.25 m, activated by an odometer wheel attached to the sled. To help remove ambient electromagnetic noise, all measurements were collected using 8 stacks per sample.

We processed all GPR data using the EKKO_Project software by Sensors & Software Inc. All data had a time-zero correction applied and then were 'dewowed' with a high-pass filter to remove low-frequency noise caused by inductive coupling effects or dynamic range limitations of the equipment (Annan, 2009). We applied a Spherical Exponential Calibrated Compensation (SEC2) time gain to all transects to compensate for signal losses due to spherical spreading and exponential energy attenuation (Annan, 2009). The SEC2 gain preserves the relative amplitude information of reflections at various depths. Transects were collected over relatively flat ground, with irregularities in the ground surface noted. Table SI1 presents the start gain, attenuation, and maximum gains used for the respective transects, as well as the co-located piezometers.

We combined processed GPR data with depth measurements of floodplain sediments based on the sediment cores to identify the physical origin of reflectors and change time-based information to depth. In Meander A, sedimentary data from four piezometers, ranging from 0.4-1.1 m depth (APZ-1 through 4; Table I), were compared to GPR data. In Meander D, sediment data from five piezometers (DPZ-1 through 5), ranging from 0.6-1.25 m depth, were used. Radar facies were classified by elements such as reflection geometry, amplitude, continuity, and degree of penetration and were ascribed to different strata and depositional features (Van Overmeeren 1998), based on previously documented GPR signatures (e.g. Vandenberghe & Van Overmeeren 1999; Kostic & Aigner 2007; Bridge 2009; Miall 2014; Słowik, 2016). Facies configurations and dimensions were also compared to visible features along the East River, including current channels and point-bars.

Paleochannel Mapping

We also connected fluvial sediment architecture to remotely identifiable surficial features using a combination of historical photography, LiDAR, and WV-2 8-band multispectral data; the latter two were collected in 2015. The WV-2 data were used to calculate Normalized Difference Vegetation Index (NDVI) and Normalized Difference Water Index (NDWI) from multispectral data. NDVI is sensitive to photosynthetic activity of plants, bare soil, and standing water, and is calculated as the ratio of the difference and the sum of near-infrared and red wavelength bands and the sum of the wavelengths (e.g. Xie *et al.* 2008). NDWI is calculated as the ratio of the difference between green wavelength bands and near-infrared and the sum of green wavelength bands and near-infrared (McFeeters, 1996). We additionally identified abandoned channels using LiDAR and NDVI, which we refer to as "paleochannels" if not in the static historical images. We used an object-oriented image-analysis software package, eCognition™ by Trimble, to classify regions that were likely occupied by former channels, using differences in vegetative and physical indicators, including: NDVI signatures, presence of ponded water, proximity to the current river channel, and elevation relative to the surrounding floodplain. We generated image-objects by merging pixels possessing similar parameter values and assigned each object to a designated class of floodplain features (such as "channel" and "surrounding floodplain"). The data with the greatest success of automatically identifying former channels—based on comparison with images from the U.S. Geological Survey, U.S. Department of Agriculture Forest Service, National Agricultural Imagery Project (NAIP), and historical aerial photographs of the floodplain dating back to 1955—were differences in NDVI and acute disparities in elevation captured in the LiDAR.

Hydraulic Conductivity and Linear Velocity Estimates

To estimate hydraulic conductivity (K), we performed a series of falling-head slug tests at each piezometer (5 tests per well) using 1 L water slugs (Table II). Methods for processing data followed that of Hvorslev (1951) for fully-submerged well screens and Binkhorst & Robbins (1998) for wells partially submerged well screens. Hydraulic conductivity was estimated by

$$K = \frac{r^2 \ln(L/R)}{2\ L\ t_{37}} \tag{1}$$

where K is the hydraulic conductivity [L/T], r [L] is the radius of the inside of the well casing, R [L] is the radius of the borehole, L [L] is the length of the well screen, and t_{37} [T] is the time it takes the water level to recover to 37% of the initial change (Hvorslev, 1951). We only used data from the mid-time, log-linear portion of slug tests to estimate local subsurface K (Binkhorst and Robbins, 1998). Additionally, for partially submerged wells, we substituted effective casing radii (r_e) and screen lengths (L_e; the length submerged under static water table conditions) for their respective counterparts in Equation (1). A representative effective casing radius r_e was calculated by

$$r_e = \sqrt{\left(r^2 + S_y\left(R^2 - r^2\right)\right)} \tag{2}$$

where S_y [-] is the specific yield of the sandpack (Binkhorst and Robbins, 1998). We utilized a representative S_y of 0.21 for the fine-medium grained sand (Johnson, 1963) used to pack the wells. The resulting effective casing radius was 2.66 cm.

Table II. Summary of hydraulic conductivity (K) estimates and standard deviation values calculated from the five slug tests per piezometer. The screened sediments are those sediment textures which the screened casing intercepted. K data not available for APZ-2

Piezometer Name	Screened Sediments	K (m/d)	Std Dev (m/d)
APZ-1	gravels and fines	0.8	4E-02
APZ-2	gravels, sand, and fines	--	--
APZ-3	gravels, sand, and fines	2	5E-02
APZ-4	gravels, sand and pebbles, and fines	0.6	5E-02
DPZ-1	gravels, sand, and fines	0.3	3E-02
DPZ-2	gravels and fines	0.2	4E-02
DPZ-3	pebbles and sands	4	3E-02
DPZ-4	pebbles, sands, and fines	0.3	5E-02
DPZ-5	sand and fines	3	3E-01

© 2019 John Wiley & Sons, Ltd.

To calculate water table gradients across each meander, we calculated three-point problems using water table elevations across all piezometer combinations within a meander. Well location and water table elevation data are in Table SI2, and various well configurations and resulting water table gradients' magnitude are in Table SI3. Using the hydraulic conductivity data and hydraulic heads from the piezometers, we estimated the average linear velocity and residence times across the meanders using Darcy's Law. We did not measure effective porosity directly so we used a representative average porosity value of 0.25, an estimate from another headwater catchment in the Rocky Mountains (Bradford *et al.*, 2009). To estimate lateral hyporheic residence times across the meander, we simply divided the estimated flow path lengths across the meander, based on a straight-line distance along the maximum hydraulic gradient, by the calculated average linear velocity.

Results

Floodplain Variability

Differences between Meanders A and D included their subsurface sedimentology, sediment structure, channel migration histories, and channel geometry. Sediment characterization from cores indicated a consistent 0.3-0.7-m layer of surficial overbank fine sediment deposits (silt) underlain by heterogeneous deposits containing gravels in Meander A (Figure 4). In contrast, Meander D's sedimentology varies and is composed of different types of sediment packages, including gravels, sands and pebbles, and fines, the spatial extent of which are localized and discontinuous (Figure 4). Fine overbank sediments are thinner (0.2-0.5 m) in sediment cores at Meander D than Meander A. Gravels in Meander D were encountered in the two cores farthest from the meander apex (DPZ-1 at 0.5 m depth and DPZ-2 at 0.5 m depth), and the remaining three sediment cores contain interbedded layers of fines, fine to coarse sand, and pebbles. Additionally, Meander D has a smaller sinuosity (2.6) compared to Meander A (6.3). Sinuosity is calculated by dividing the longitudinal length of the river along the midline by the shortest distance between apexes at the meander neck (Rosgen, 1996). The average sinuosity of the East River channel in the upper catchment (Figure 2) is 1.8. Relevant to the residence time of lateral groundwater flow, Meander D is oriented down-valley, with groundwater gradients oriented subparallel to the greater valley gradient, while Meander A is oriented across-valley, with groundwater flow across the meander, orthogonal to the valley-gradient. Meander D also has a greater wavelength: ~60 m versus ~30 m, respectively (Figure 3), which is an important metric when considering lateral groundwater movement or hyporheic exchange across the meanders.

Comparing the East River's migration history along reaches near each meander also helps elucidate resulting differences between the meanders' stratigraphy. This exercise provides spatial context of the current channel geometry, relative to former channel migration and other geomorphic features, such as former cutoffs, alluvial-fans, and valley walls. We tracked the migration of the East River using historical images dating back to 1955 and identified likely paleochannel locations using the multifaceted mapping approach (Figure 5). A key event in the East River's local migration was the development of the 2007 cutoff, just upstream of Meander D. Initiation occurred in approximately 2007, and major flow diversion to the chute occurring approximately in 2012. Another significant feature is the progressive lateral channel migration of Meander A, increasing Meander A's sinuosity, while maintaining its sinusoidal shape. In contrast, Meander D's channel has been relatively confined over the past sixty years and did not exhibit considerable lateral channel migration. Combined NDVI, NDWI, and LiDAR-based elevations identified abandoned channels proximal to the study meanders (grey; Figure 5).

GPR Radar Facies

The East River GPR datasets exhibited four distinct fluvial radar facies: a) former channels; b) lateral accretion structures; c) point-bars; and d) heterogeneous gravel layers (Table III, Figure SI1). The recognized radar facies are usually present in meandering river settings (Bridge, 2009; Miall, 2014) and outlined in detail here.

Former channels are indicated by bright, concave-up bottom reflectors, overlain by less-distinct, sub-horizontal layers

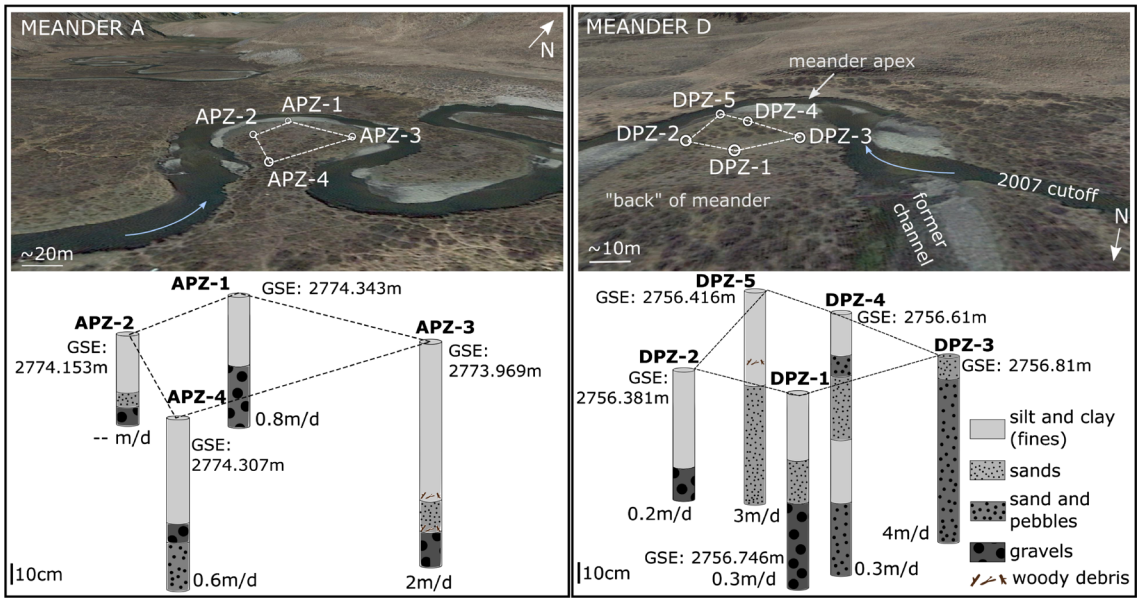

Figure 4. Sediment cores and hydraulic conductivity estimates. Oblique views looking down each meander. Depths are to scale. Core widths are not to scale to show details. Hydraulic conductivity is displayed in m/d. K data are not available for APZ-2 due to equipment failure. Ground-surface elevation (GSE) is in meters above mean sea level. [Colour figure can be viewed at wileyonlinelibrary.com]

© 2019 John Wiley & Sons, Ltd.

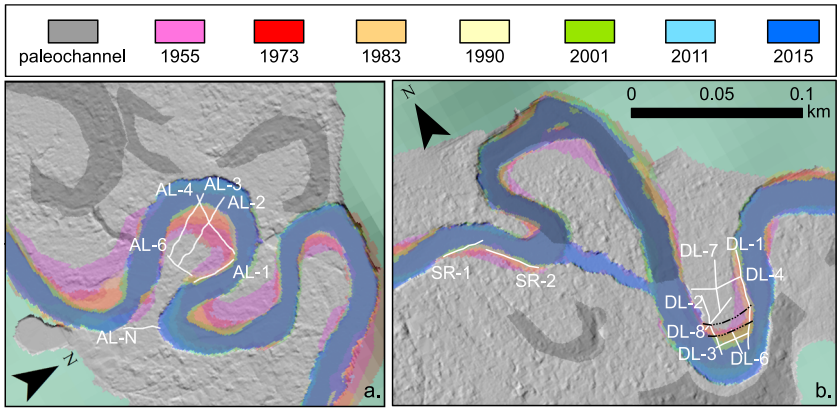

Figure 5. The migration of East River. Overlay of LiDAR; former channel locations, abandoned post 1955 (rainbow); paleochannels based on NDVI and elevation (grey); GPR transects (white lines); and interpreted former channel at Meander D (dashed black lines). Scale bar applies to both panels a and b. [Colour figure can be viewed at wileyonlinelibrary.com]

Table III. Descriptions of GPR reflection patterns, associated sedimentary structures, and locations in depicted transects

Reflection pattern- radar facies	Sedimentary stucture or feature	Illustrated in figure
Bright, concave-up reflector (channel bottom) and weaker, subhorizontal, linear reflectors (channel fill)	abandoned channel	Figure 6, transect SRL-2 (~17-32 m) Figure 8, transect DL-1 (~32-42 m)
Subparallel reflectors, dipping in the direction of accretion	lateral accretion structure	Figure 8, transect DL-1 (~28-34 m)
Bright, convex-up reflectors	point bar	Figure 6, transect SRL-1, (~12-24 m) Figure 8, transect DL-1 (~20-34 m) Figure 8, transect DL-2 (~14-18 m) Figure 8, transect DL-8 (~18-22 m)
Discontinuous, hummocky reflectors, and diffraction hypoerbolae	heterogeneous gravel layer	Figure 7, transect AL-2 (~8-13 m, ~24-28 m, and ~44-50 m) Figure 7, transect AL-4 (~24-36 m)

(Van Overmeeren 1998; Vandenberghe & Van Overmeeren 1999; Ekes & Hickin 2001; Skelly *et al.* 2003; Słowik 2016). The concave-up reflector demarcates the channel bottom, and the stark reflection at the channel base occurs due to the juxtaposition of coarser-grained bed layer and finer-grained sediments related to channel fill, which have contrasting dielectric permittivity (e.g. Vandenberghe & Van Overmeeren 1999; Bridge 2009). Flooding and high flows, such as those associated with peak snowmelt in this region, are a driving force behind abandoned meander infilling. It may take many flood events to infill a channel; therefore, the fine-grained fill layers may also be weakly laminated (Toonen *et al.*, 2012). In our GPR data, we saw weak, sub-horizontal, linear reflectors in channel deposits, associated with fine-grained sediments and attributed to laminated fill structures (Figure SI1a; e.g. Toonen *et al.*, 2012).

Lateral accretion structures are imaged as subparallel reflectors that dip in the direction of aggradation (Table III; Vandenberghe & Van Overmeeren 1999; Kostic & Aigner 2007; Słowik 2016), and can indicate the direction of structure migration (Bridge, 2009; Toonen *et al.*, 2012). In meandering systems, aggradation structures may be paired laterally, across the channel, with erosional features, such as basal channel scour or cutbanks (Bridge, 2003; Miall, 2014; Toonen *et al.*, 2012). This lateral pairing of erosion and deposition was noted across the current East River channel and was imaged in GPR transects at Meander D (Figure SI1b). The signature of an erosive cutbank—an acute transition between GPR patterns—is seen at 42 m on the transect DL-1. Here, sub-horizontal linear reflections meet hyperbolae from point reflectors.

The top outline of point-bars are indicated by convex-up reflectors created by the contrast of coarser point-bar material mantled by finer-grained sediments (Figure SI1c; Bridge, 2003; Miall, 2014). Due to potential variation within point-bar deposits and the lack of clear internal structures in the East River GPR data, we utilized two key features to identify point-bars: 1) the convex-up reflector shape, both laterally and longitudinally with respect to the related channel, and 2) the amplitude of this reflection, likely caused by contrasting sediment types of the gravel point-bar and on-lapping finer sediments (Bridge *et al.*, 1995; Miall, 2014; Słowik, 2016).

Heterogeneous gravel layers are characterized by discontinuous and hummocky reflectors (Figure SI1d). Although fragmented, the reflectors can be very bright and generate numerous diffraction hyperbolae, commonly attributed to gravel, cobbles, or boulders (Van Overmeeren, 1998). The convolution of many hyperbolae creates a rugose appearance to the layer, although individual hyperbola are also visible. At our site, hyperbolae correlated to the presence of gravels seen in sediment cores. The lack of distinct and continuous reflectors, as well as the appearance of multiple hyperbolae, characterized this facies type in the East River and indicated heterogranular deposits that contain gravels.

Meander sediment architecture

We interpreted internal meander sediment architecture by combining GPR and sediment core data with channel migration histories. For example, in the SR-2 transect on the 2007 cutoff, we imaged the subsurface portions of a current point-bar and a former channel using GPR (Figure 6). By overlaying the SR-2 GPR transect with channel locations indicated from historical imagery (Figure 5b), we corroborated the imaged channel with a former channel. The imaged channel in SR-2 is ~1 m deep and ~15 m wide, similar to the current river's

© 2019 John Wiley & Sons, Ltd.

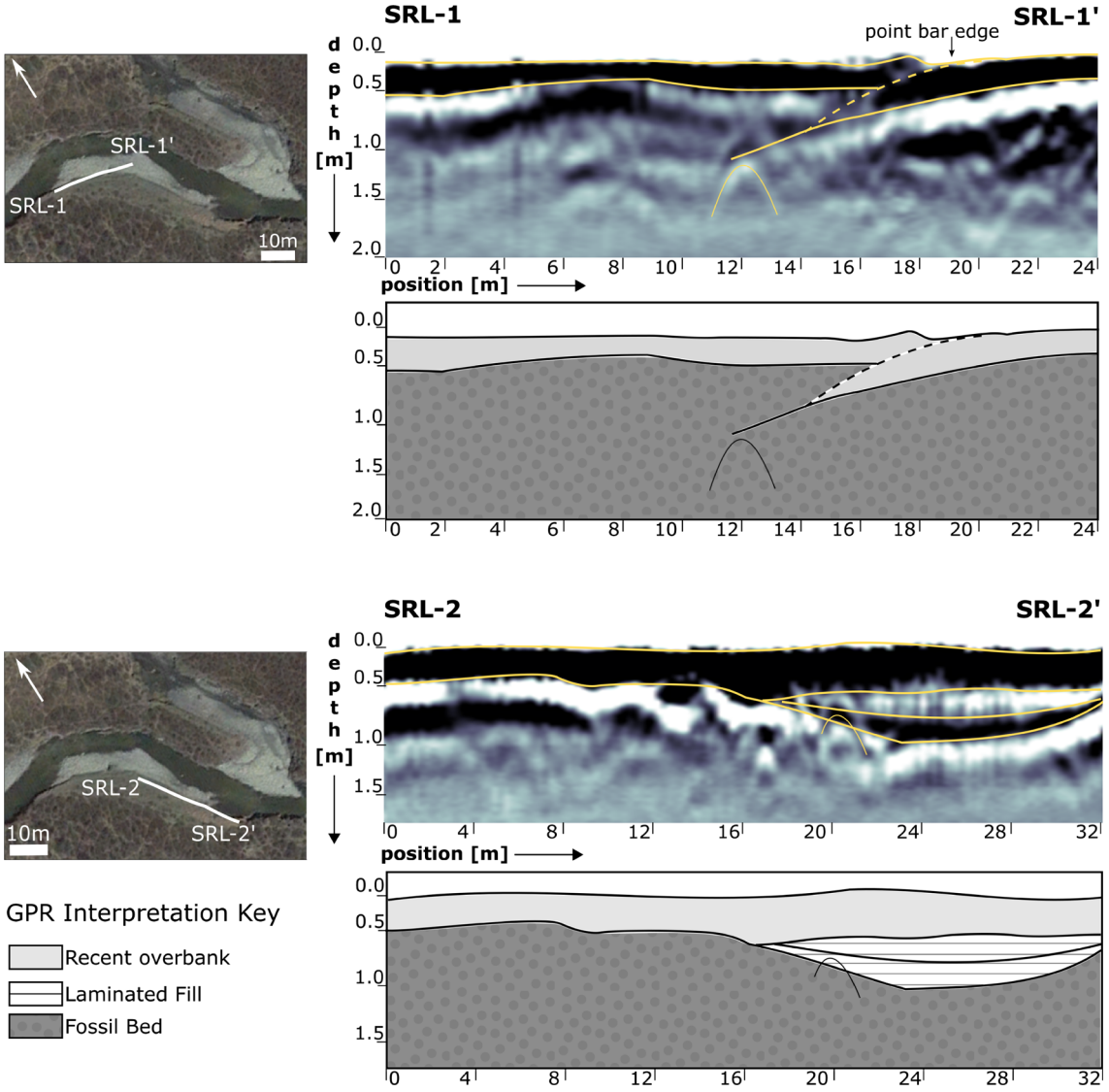

Figure 6. GPR transects along the straight reach. Yellow lines call out features. Depth and horizontal location (position) are in meters. The term "fossil bed" refers subsurface sediments or bedrock not related to recent river migration and which do not present clearly discernable reflectors (Toonen et al., 2012). [Colour figure can be viewed at wileyonlinelibrary.com]

dimensions. However, it is unclear if the SR-2 transect ran laterally across the former channel, so we compared the former channel's width with current dimensions cautiously. Average active-channel widths along Meander A and D at the time of the study were 9 and 12 m, respectively, and average bankfull widths were 18 and 36 m, respectively. Additionally, GPR imaged the buried portion of the coarsely grained point-bar in SR-1. The proximity of the point-bar and overlying overbank fines, as well as the concave-up channel filled with fines, exhibits the acute structural heterogeneity created by the various bedforms preserved in the East River floodplain via river migration and channel abandonment.

As noted earlier, Meander A is simpler in its stratigraphy than Meander D. Although the boreholes were relatively shallow (<1 m), all cores from Meander A contained gravels at their base, and GPR facies indicate that gravels continued to depths up to ~1.8 m across the length and width of Meander A (Figure 7; Figure SI2; Figure SI3). Gravels measured at the cutbank of the meander's neck additionally corroborate the GPR signatures of the gravel deposits, which range from rugose reflectors to hyperbolae (Figure SI3).

Sedimentological differences and a sequence of GPR facies support the interpretation of variable depositional regimes across Meander D. The heterogranular GPR facies (Figure SI1d) were only imaged toward the back of the meander (transects DL-1, DL-2, DL-7; Figure SI4) and were corroborated with the boreholes (Figure 8; DPZ-1 and DPZ-2) as a continuous heterogranular gravel layer overlain by overbank fines. Towards the apex of the meander, gravels were absent, and the boreholes revealed interbedded layers of fines and sands. The termination of the heterogranular gravel deposit was collocated with the end of a convex-up point-bar reflection, seen in GPR transects DL-1, DL-2, DL-7, and DL-8 (Figure 8; Figure SI4). In transect DL-1, reflectors indicate lateral aggradation towards the apex of the meander (Figure 8). These bright, dipping reflectors suggest a strong contrast between the gravel deposit and finer-grained sediments towards the meander apex. Fine-grained channel fill is located in the middle of the transect. A 10-15 m wide swath of poorly defined, sub-horizontal reflectors appeared in GPR transects DL-1, DL-2, DL-6, and DL-8 (Figure 8; Figure SI4) and possibly represents laminated fill. Along this line, sediment cores from piezometers DPZ-4 and DPZ-5 included layers of sands and fines, and pieces of organic matter and branches (Table I; Figure 4). Lastly, there is an abrupt transition from the fine-grained fill to a layer of gravels associated with the current point-bar at the apex of Meander D (Figure 8). This transition can be seen in transects DL-1, DL-2, and DL-6 and may reflect an erosional feature. The sequence

© 2019 John Wiley & Sons, Ltd.

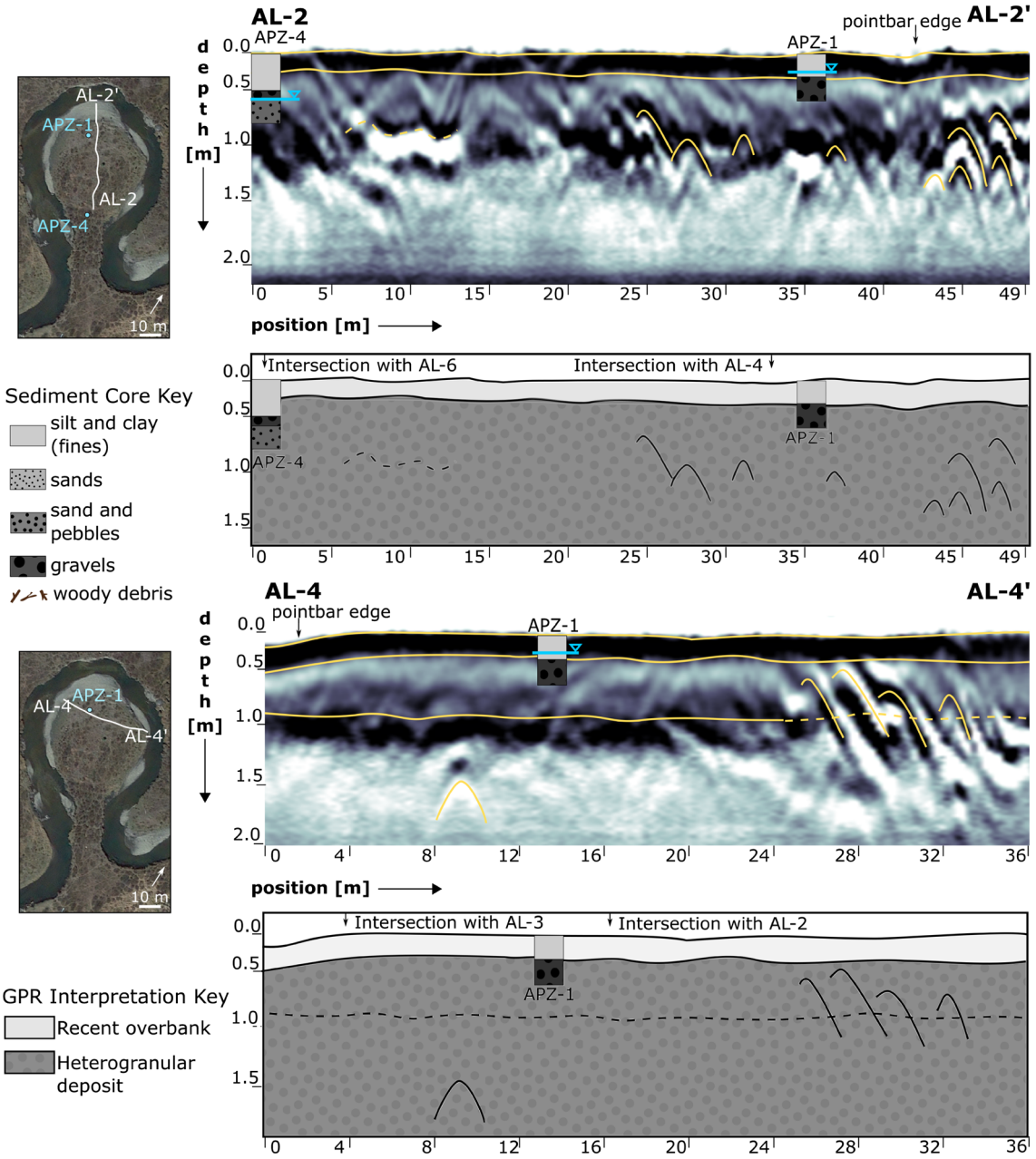

Figure 7. Representative GPR transects of Meander A. Additional transects in supplemental information. Blue lines indicate water table. Yellow lines mark key features. Hyperbolae related to gravels are mapped laterally and longitudinally across the meander (Figures SI2 and SI3). Depth and horizontal location (position) are in meters. [Colour figure can be viewed at wileyonlinelibrary.com]

of point-bar, accretion, fill, and erosional GPR facies down the meander indicates that the deposits are laterally discontinuous, and reflect disparate depositional regimes across the meander.

Hydraulic Conductivity, Gradients, and Linear Velocity

Differences in sedimentology between and within meanders do not appear to translate to a large range of hydraulic conductivity (K), as measured via slug tests; the geometric means of K values for Meander A and Meander D are 1 and 0.7 m/d, respectively (Table II). Meander A's K values differed from one another by less than an order of magnitude, and Meander D's by just over an order of magnitude. The low variance in K values may be attributed to the fact that the piezometers' screened intervals cover multiple sediment types such that the measured values reflect an average of the screened sediments rather than an estimate of one discrete sediment package. Additionally, slug tests can be biased by altered, low-K materials near the well (Butler and Healey, 1998; Rovey and Niemann, 2001), and because they do not stress the aquifer, produce smaller effective test areas with lower K estimates (Rovey and Cherkauer, 1995; Rovey and Niemann, 2001) and lower variance (Bohling *et al.*, 2012; Rovey and Cherkauer, 1995) than other methods, such as direct push or pumping tests. Therefore, the K values reported here may serve as a rough estimate of an effective K for the East River meanders, but cannot conclusively characterize the different sediment facies without additional and alternative K measurements.

The direction of the hydraulic gradients in both meanders differed between the snowmelt-dominated flow regimes of late spring/early summer and the near-baseflow conditions of later summer. At Meander A, the direction of the gradient shifts seasonally but was of similar magnitude (~0.01) through time (Figure 9; Table SI3). River discharge is greatest in early summer (~15m^3 vs 1m^3 in fall and winter). The orientation of discharge,

© 2019 John Wiley & Sons, Ltd.

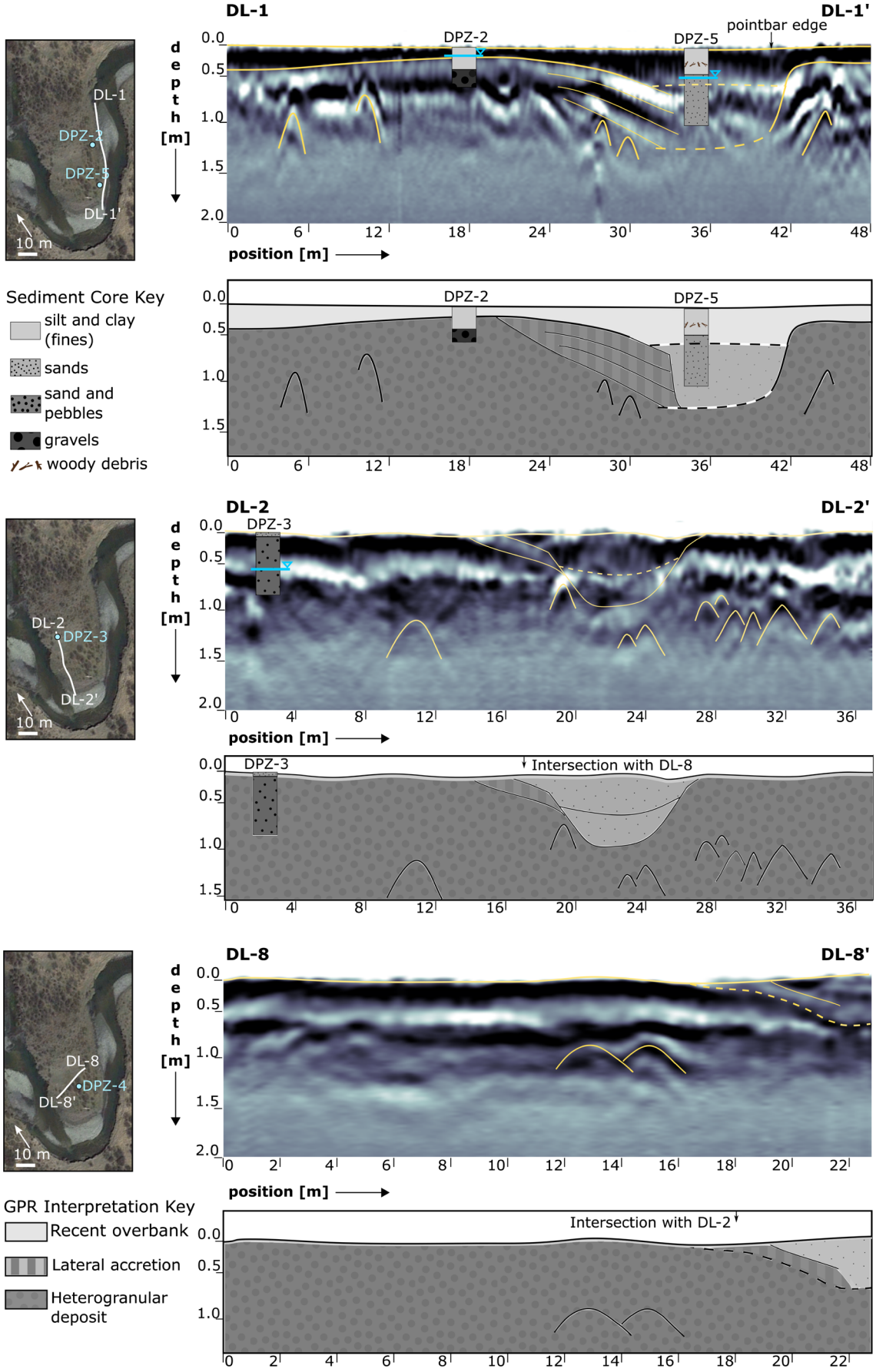

Figure 8. Key GPR transects of Meander D. Additional transects in supplemental information. Blue lines indicate water table. Yellow lines mark key features. Depth and horizontal location (position) are in meters. [Colour figure can be viewed at wileyonlinelibrary.com]

along with snowmelt inputs from valley walls, potentially created the cross-valley flow across Meander A in the early season. Late in the season, down-valley base flow was likely a large contribution to river discharge (Winnick *et al.* 2017).

© 2019 John Wiley & Sons, Ltd.

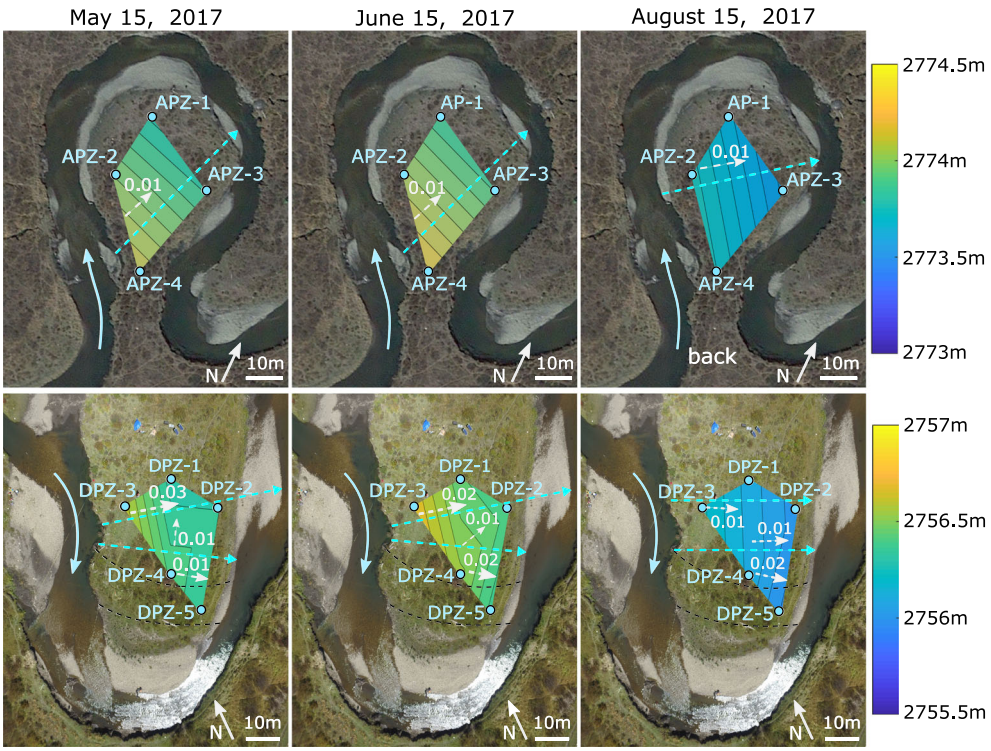

Figure 9. Water table elevations (in color, meters above sea level) and gradient estimates for the two meanders during late spring (left), early summer (middle), and later summer (right), 2017. Meander A (top row) has its meander apex towards the top of the images, while Meander D has its apex towards the bottom of the image. White dashed lines are the raw calculated water table gradients. Blue lines indicate estimated flow paths across the meander. Dashed black lines at Meander D are the estimated boundaries of channel sediments. [Colour figure can be viewed at wileyonlinelibrary.com]

Hyporheic residence times in Meander A likely vary more as a function of flow-path direction and length than changes in seasonal hydraulic gradient (Table IV).

At Meander D, the dominant water table gradient direction was down-valley, but there was variability in the water table elevation across the meander (Figure 9; Table SI3). This variability was greatest in the early season, as depicted by bidirectional flow across the meander as estimated by differing well triads; this may have been related to the surface-water flow concentrated by the 2007 cutoff towards the upstream portion of Meander D (near DPZ-3). The largest hydraulic gradient observed across Meander D (0.03) occurred in early summer, concomitant with peak snowmelt and surface discharge. Later in the season, the largest hydraulic gradient was near the apex of the meander (0.02). The largest estimated hydraulic gradients related to the fastest linear velocity calculations and shortest residence times of water flowing across the meander, but the direction of the gradient influenced the flow-path length estimates (Figure 9; Table IV). The shortest lateral hyporheic residence time estimate for Meander D was 500 days, but this estimate occurred both in May with larger gradient (0.03) and longer flow-path length (45 m), and later in the season with lower gradient (0.02) and shorter flow paths (30 m); Figure 9).

Discussion

Although Meanders A and D share sediment sources and have similar vegetation, channel discharge, and slope, their respective migration histories and associated erosional/depositional processes have impacted their sediment architecture. In turn, these differences in floodplain hydrofacies heterogeneity and connectivity may control intra-meander hydrologic processes, such as groundwater transport or lateral hyporheic exchange. Here, we discuss differences in Meander A and Meander D's evolution and geomorphic context, the resulting key features of their shape and stratigraphy, and impacts on hydrologic processes.

Floodplain Evolution and Meander Stratigraphy

Meander A evolved via progressive lateral river migration, where the channel migrates outwards and erodes its cutbanks (Figure 5a; Figure SI5), while depositing coarser material on the inside of the meander bend. Historical images captured this migration, which is also supported by the meander's sedimentology and stratigraphy. Progressive lateral migration of the East

Table IV. Estimates of flow path lengths (Figure 9), average linear velocities (v), and residence times. Geometric means of K estimates, used for Meander A and Meander D are 1 and 0.7 m/d, respectively. The hydraulic gradient value used for Meander A's velocity estimate was 0.01. For Meander D hydraulic gradients used were estimated using the piezometer triads DPZ-1, -3, and -4, and DPZ-2, -4, and 5, respectively (Table SI3, values in bold)

Using the Geometric mean of K	Meander A		Back of Meander D			Apex of Meander D		
	May/June	August	May	June	Aug	May	June	Aug
flow path length [m]	50	40	45	45	40	30	30	30
v [m/d]	0.04	0.04	0.08	0.06	0.03	0.03	0.06	0.06
$t_{residence}$ [d]	1300	1000	500	800	1400	1000	500	500

© 2019 John Wiley & Sons, Ltd.

River and point-bar aggradation (Figure 5a) would have erased evidence of earlier channel locations, leaving coarse point-bar deposits, overlain by overbank fines observed across Meander A. Lateral river migration's depositional processes result in increasing sinuosity, thin meander necks, and a relatively homogenous sediment architecture of aggraded coarse sediments. The stratigraphic result of lateral migration is that Meander A does not appear to have any major sediment structures across the floodplain.

In contrast, Meander D's varied sedimentology and stratigraphy indicates an evolution punctuated by disparate depositional regimes, rather than progressive lateral migration. Key components of the meander's sedimentology are coarser, heterogranular deposits at the back and near the current point-bar of the meander, with an intervening deposit of fine-grained sediments. These fines are collocated with a linear trough-shaped reflection in GPR, laterally located across the meander. This feature may represent a secondary channel structure across the meander, such as a swale, or a minor chute that failed and subsequently filled in. Swales, which are near-channel depressions occupied during overbank flow, as well as failed chute structures, represent lower flow regimes and are associated with fine-grained deposits (Toonen *et al.*, 2012). Unstable flow regimes, unsteady sediment inputs, and bend geometry can divide river discharge, leading to channel bifurcation and chute formation near meander apexes (i.e., bifurcated chute or double-headed meander; Van Dijk *et al.*, 2014). However, bifurcated chutes have a high rate of failure, relative to bend and neck cutoffs, due to sediment-discharge dynamics and gradient advantages (Van Dijk *et al.* 2017). Disconnection from the main channel, for chutes by failure and infilling, and for swales during waning flood stages, reduces flow and erosive power and allows for sediment deposition and preservation of channel features. Former chutes or swales may only be occupied by the river during overbank flow, and flow in these secondary channels is lower and slower, not capable of moving coarser channel bed sediment. Instead, lower flows in abandoned chute and swale structures are associated with deposition of finer sediments, and deposition over the former channel shape preserves the channel (Toonen *et al.* 2012). The preserved secondary channel structure at Meander D and the fine-grained fill (seen at ~30-42 m along transect DL-1; Figure 8) may indicate that flow became disconnected from the secondary channel at some point and was active only during high flows. The secondary channel structure runs laterally across Meander D, parallel to the greater valley gradient.

Floodplain Structures and Heterogeneity

K estimates from slug test data across the study site only vary approximately an order of magnitude difference across both meanders and all sediment types. However, when combined with water table gradients, flow-path lengths, and strata connectivity as estimated by the GPR and remotely sensed data, linear transport velocities and lateral hyporheic residence time estimates across the meanders are quite different. Across Meander A, hydraulic gradients are low and do not change greatly throughout the data collection period, likely owing to Meander A's geometry and orientation across-valley (Figure 9). GPR and sediment cores support a simplified stratigraphy devoid of structures with disparate sedimentologies. Despite these homogeneities, residence times across the meander, based on a geometric mean of K values of 1 m/d, likely vary widely due to the meander's high sinuosity (Figure 10a). Lateral hyporheic residence time estimates in Table IV reflect transport across the widest part of the meander (~50 m wide); if we consider flow paths across Meander A's (~20 m wide) neck instead, estimated hyporheic residence times in early season drop from 1300 to 500 days.

We estimated the linear velocities and residence times at Meander D using a geometric mean of K values (0.7 m/d). However, depending on orientation of fluvial packages, higher K strata can create preferential flow paths, increasing the meander's effective K and linear flow velocities (Figure 10b). Across Meander D, the largest K values are located near the preserved former chute (DP-3 and DP-5; Figure 4), which is oriented down-valley, parallel to the groundwater gradient (Figure 9). Considering an arithmetic mean of Meander D's K values (1.6 m/d), which is perhaps appropriate given the orientation of packages with respect to the gradient, linear velocity estimates double and residence times are halved (Table V). Even given the narrow range of estimated K values at this site based on available data, there may be a significant difference in estimated linear velocity when strata orientation is considered. This finding illustrates the importance of capturing the range of hydraulic conductivities related to fluvial strata as well as strata connectivity and orientation in physical hydrologic models. Doubling of residence time can have an important impact on estimates of hyporheic efficacy in transforming solutes (e.g. Bardini *et al.* 2012; Gomez-Velez & Harvey 2014; Gomez-Velez *et al.* 2015).

A key goal of our study was to document how specific mechanisms of river migration result in different hydrofacies and therefore affect hydrologic processes. For example, the former channel in our study site at Meander D is oriented so that it likely increases effective hydraulic conductivity and groundwater flux, and decreases residency times of lateral hyporheic waters (Figure 10b). Alternatively, in the event of a neck cutoff and meander abandonment, the river gradient will increase significantly, resulting in increased longitudinal (vertical) hyporheic exchange below the current channel bed (Boano *et al.*, 2007, Figure 10c). However, this process will also significantly reduce lateral hyporheic exchange that had occurred across the meander, because of the resulting flow configuration (Boano *et al.*, 2006; Revelli *et al.*, 2008). Alternative scenarios might reduce the effective hydraulic conductivity across the meanders and increase residency times of laterally exchanged hyporheic waters. For example, if river discharge is reduced long-term, either by a dam or irrigation outtake, stream power decreases. The reduction in stream power would result in deposition of finer sediment and infilling (Figure 10d). Along a meander, channel infilling would reduce the connectivity of the stream channel to coarser meander sediments, creating a decrease in effective hydraulic conductivity and average groundwater velocity, and an increase in residence times of laterally exchanged hyporheic waters.

Mapping Abandoned Channels and Strata at the Floodplain Scale

Subsequent surficial expressions of river evolution offer a direct link between river migration and patterns in floodplain heterogeneity and strata connectivity (Figure 10). Leveraging remote methods of mapping former channel locations may offer an efficient way of mapping and integrating key hydrostratigraphic elements into hydrologic models. In addition to historical imagery, we augmented the body of recognizable former channels (paleochannels) by combining LiDAR-based elevation and NDVI data to identify elevation differences and land-cover disparities related to gradual infilling and vegetative succession of abandoned channels (Figure SI6). Although this technique is

© 2019 John Wiley & Sons, Ltd.

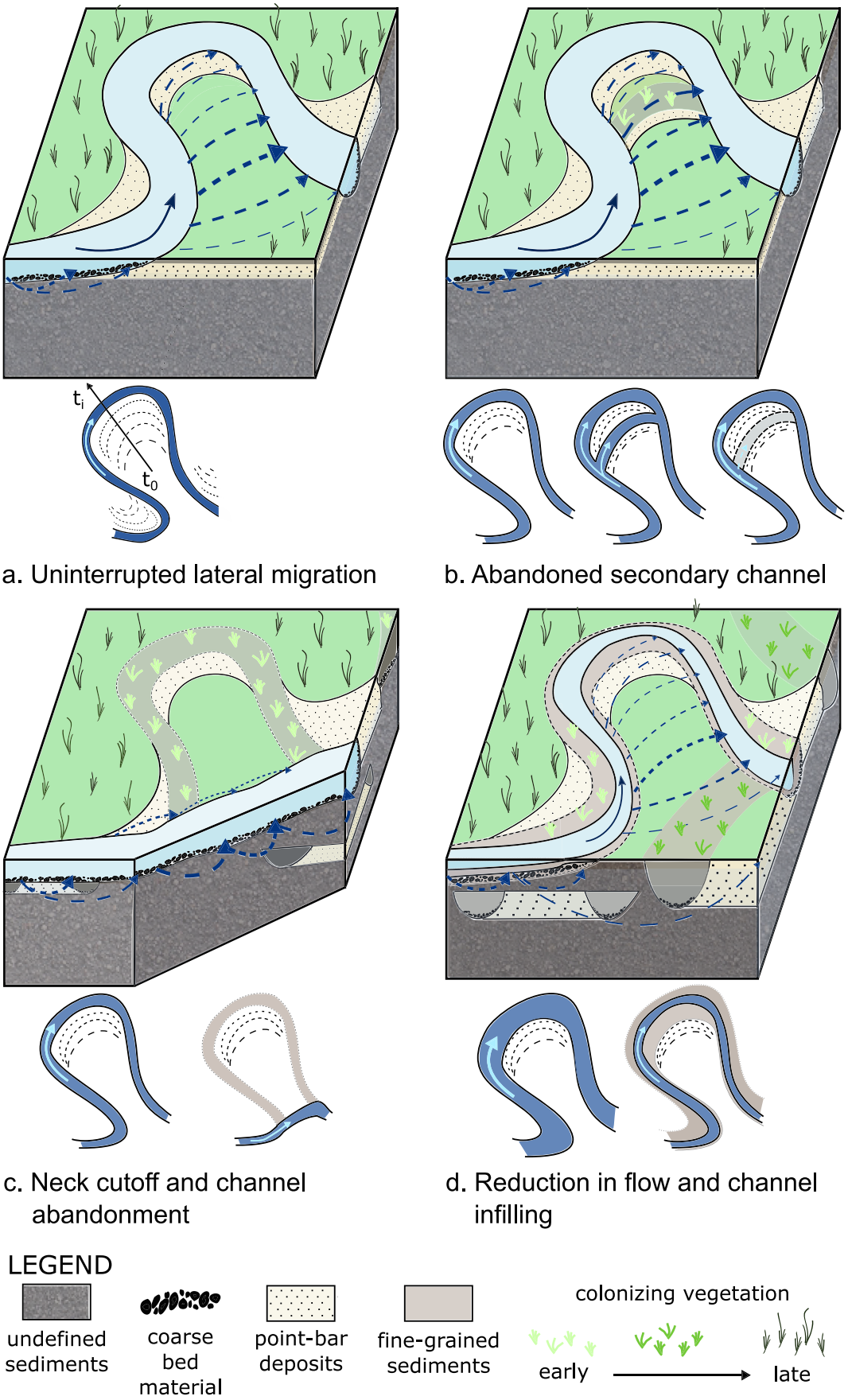

Figure 10. Conceptual cartoons of different river evolutions; resulting sediment structures surficial features, and successional vegetation distributions; and the effects on vertical and lateral hyporheic exchange. Arrows denote theoretical, relative hyporheic residence times. 10a: A meander planform created by uninterrupted lateral migration. Meander sediment structure is relatively homogeneous, lacking stark, hydrostratigraphic contrasts. 10b: Meander sediment structure and hyporheic flow paths resulting from a former secondary channel. Vegetation is beginning to recolonize the abandoned channel. 10c: Resulting effects on lateral and vertical hyporheic exchange caused by a meander neck cutoff. Figure is cut away to show the channel bottom after the neck cutoff. Neck cutoffs increase the river gradient leading to an increase in vertical hyporheic exchange (e.g. Wondzell, 2006). 10d: A complex floodplain, showing various hydrostratigraphic elements caused by river migration and resulting vegetation distributions. [Colour figure can be viewed at wileyonlinelibrary.com]

© 2019 John Wiley & Sons, Ltd.

Table V. Comparison of linear velocity and residence time estimates of groundwater flowing laterally across Meander D using geometric (0.7 m/d; top) and arithmetic (1.6 m/d; bottom) means of K values

Meander D	Back of Meander			Meander Apex		
using AVG_{geo} K	May	June	August	May	June	August
flow path length [m]	45	45	40	30	30	30
v [m/d]	0.08	0.06	0.03	0.03	0.06	0.06
$t_{residence}$ [d]	500	800	1400	1000	500	500
using AVG_{arthm} K	May	June	August	May	June	August
flow path length [m]	45	45	40	30	30	30
v [m/d]	0.19	0.13	0.06	0.06	0.13	0.13
$t_{residence}$ [d]	200	400	600	500	200	200

efficient and portable, it has limitations, including the need for human input to adjust the parameter thresholds indicative of a channel and to refine channel boundaries when one attribute may overshadow others. This is necessary particularly where vegetation shadows channel margins and or hyperspectral bands do not distinguish difference in bar sand and gravel from dry vegetation. However, once thresholds are set, the software can be applied to the entire floodplain.

Although former channel locations can be mapped using traditional methods, including topographic maps and static remote images, this approach relies solely on human input, without the prospect of further automation or increases in efficiency. It should also be stated that the current requirement of manual adjustments of our proposed method does not preclude future improvement of the technique's automation. The assimilation of the various datasets within the eCognition software as well as the ability to calibrate the floodplain parameter classification facilitates the methods flexibility and portability to a range of watersheds. In fluvial settings with steady flow conditions, shallow river gradients, and minimal topography, such as dispositional reaches of larger rivers, successive vegetation might be the key parameter to identify former channel locations. Although we have not applied our method to lower energy environments, such as higher stream order, lower gradient, depositional environments, other studies have examined and documented vegetative succession in lower- energy environments (Greco *et al.*, 2007; Greene and Knox, 2014)**.** Alternatively, in instances where vegetative differences are subtle, LiDAR may be key. However, our approach may be less useful in floodplains with smaller ranges in sediment sizes, and therefore potentially smaller contrasts in hydraulic conductivity. In such settings, hydrostratigraphic packages related to river migration will have more consistent hydraulic characteristics. An example of this setting is at the mouth of larger rivers, with minimal gradients, reduced stream power, and bed sediments dominated by sand. Here, mapping sediment architecture might be less helpful in determining hydrologic preferential pathways, due to minimal contrasts in hydraulic conductivity of the strata.

Applications of remote hydrostratigraphy mapping

An exciting potential use of our approach to mapping key hydrostratigraphic elements is in contaminant transport applications. Across a spectrum of contaminants and alluvial settings, estimating hydraulic connectivity of alluvial sediments remains a critical study parameter for understanding contaminant transport and storage (both physical and chemical) processes, timing of pollution migration, and efficacy of remediation efforts (e.g. Fuchs *et al.*, 2009; Heeren *et al.*, 2010, 2011; Mulligan and Uchupi, 2003; Stollenwerk and Grove, 1985; Zhang *et al.*, 2013). Alluvial aquifers are vulnerable to contamination—from agricultural by-products, bacteria, nutrient loading, acid mine drainage, and heavy metals (both natural and anthropogenic), for example—posing environmental and human health risks. Mapping contaminant flow paths and flow rates in floodplains may be critical to mitigating future environmental disasters, such as the Gold King Mine waste water spill (Silverton, Colorado) in 2015 (EPA, 2017). Studies limited in time or funding might benefit from our remote approach to mapping hydrofacies. Although additional testing is needed, our method is based on well-documented surficial features of former channels, associated stratigraphy and sediment sequences, and relative characteristics of key hydrofacies (higher K channel bottoms and point bars, lower K channel fill and overbank deposits). This approach to mapping hydrofacies could serve as a cost- and time-efficient estimates of floodplain heterogeneity and contaminant flow paths.

Conclusions

The location, extent, and orientation of hydrofacies can have a large impact on physical and chemical hydrologic processes, and an efficient way of mapping hydrofacies and floodplain heterogeneity can help inform hydrological and geomorphological studies. In this study, we examined the stratigraphy and hydrology of two meanders with contrasting geometries in a subalpine floodplain using sediment cores, slug test data, water level data, GPR, and a novel remote-sensing technique of estimating the locations of key hydrofacies.

Our results highlight risks related to using a homogeneous grain size and hydraulic conductivity to physically represent an alluvial aquifer and demonstrate effects on estimated lateral hyporheic residence times. Although the two meanders shared a sediment source, vegetation, and climate, their divergent river migration histories resulted in contrasting meander hydrofacies. In turn, the extent and orientation of these facies controlled the effective hydraulic conductivity and, ultimately, estimates of groundwater transport and hyporheic residence times. Additionally, the meanders' orientation relative to the valley gradient impacted the hydraulic gradient across the meanders—a key control of groundwater velocity. Ideally, this study provides a pathway to efficiently mapping the extent and orientation of fluvial hydrofacies using surficial floodplain characteristics, and assesses the possibility of simplifying floodplain stratigraphy into hydrostratigraphic packages for use in hydrologic and contaminant transport models.

Acknowledgements—This material is based upon work supported through the Lawrence Berkeley National Laboratory's Watershed

© 2019 John Wiley & Sons, Ltd.

Function Scientific Focus Area and the National Science Foundation (GRFP-2014183364). The U.S. Department of Energy (DOE), Office of Science, Office of Biological and Environmental Research (BER) funded the work under contract DE-AC02-05CH11231 (Lawrence Berkeley National Laboratory; operated by the University of California). Additional support was provided by DOE, Office of Science, BER, Subsurface and Biogeochemical Research program funded Early Career Award to J. Rowland. Any findings and conclusions or recommendations expressed in this material are those of the author(s) and do not necessarily reflect the views of the National Science Foundation or the DOE. Many thanks to Fiona Kirkby and the three anonymous reviewers for their thoughtful and constructive feedback. We would also like to sincerely thank Jackie Randell, Corey Lawrence, Julia Hawn, Kass Ulmer, Aspen Anderson, and John Lunzer for field assistance; Ro Carroll, Mike Gooseff, Baptiste Dafflon, and Emmanuel Léger for feedback on experimental design; and Rocky Mountain Biological Laboratory for accommodations and logistical support. Additional thanks to James Irving for technical advice with GPR processing and interpretation.

References

Allen JRL. 1970. A quantitative model of grain size and sedimentary structures of lateral deposits. *Geological Journal* **7**: 129–146.

Andrews ED. 1984. Bed-material entrainment and hydraulic geometry of gravel-bed rivers in Colorado. *Geological Society of America Bulletin* **95**: 371–378.

Annan AP. 2009. Electromagnetic Principles of Ground Penetrating Radar. In *Ground Penetrating Radar Theory and Applications*, Jol HM (ed). Elsevier Science: Amsterdam, Netherlands; 1–40.

Argiroff WA, Zak DR, Lanser CM, Wiley MJ. 2017. Microbial Community Functional Potential and Composition Are Shaped by Hydrologic Connectivity in Riverine Floodplain Soils. *Microbial Ecology* **73**: 630–644.

Bardini L, Boano F, Cardenas MB, Revelli R, Ridolfi L. 2012. Nutrient cycling in bedform induced hyporheic zones. *Geochimica et Cosmochimica Acta* **84**: 47–61.

Battin TJ, Kaplan LA, Findlay S, Hopkinson CS, Marti E, Packman AI, Sabater F. 2008. Biophysical controls on organic carbon fluxes in fluvial neworks. *Nature Geosciences* **1**: 95–100.

Bätz N, Colombini P, Cherubini P, Lane SN. 2016. Groundwater controls on biogeomorphic succession and river channel morphodynamics. *Journal of Geophysical Research* **121**: 1763–1785. https://doi.org/10.1002/2016JF004009.

Bencala KE. 1993. A perspective on stream-catchment connections. *Journal of the North American Bethnological Society* **12**: 44–47.

Bertoldi W, Gurnell AM, Drake NA. 2011. The topographic signature of vegetation development along a braided river: Results of a combined analysis of airborne lidar, color air photographs, and ground measurements. *Water Resources Research* **47**: 1–13. https://doi.org/10.1029/2010WR010319.

Binkhorst GK, Robbins GA. 1998. Conducting and interpreting slug tests in monitoring wells with partially submerged screens. *Ground Water 1* **36**: 225–229.

Boano F, Camporeale C, Revelli R, Ridolfi L. 2006. Sinuosity-driven hyporheic exchange in meandering rivers. *Geophysical Research Letters* **33**(18).

Boano F, Revelli R, Ridolfi L. 2007. Bedform-induced hyporheic exchange with unsteady flows. *Advances in Water Resources* **30**: 148–156. https://doi.org/10.1016/j.advwatres.2006.03.004 [online]

Boehlke JK, Antweiler RC, Harvey JW, Laursen AE, Smith LK, Smith RL, Voytek MA. 2009. Multi-scale measurements and modeling of denitrification in streams with varying flow and nitrate concentration in the upper Mississippi River basin, USA. *Biogeochemistry* **93**: 117–141 https://doi.org/10.1007/s10533-008-9282-8.

Bohling G, Liu G, Knobbe S, Reboulet EC, Hyndman DW, Dietrich P, Butler JJ. 2012. Geostatistical analysis of centimeter-scale hydraulic conductivity variations a the MADE site. *Water Resource Research* **48**: W02525.

Boulton AJ, Findlay S, Marmonier P, Stanley EH, Valett HM. 1998. The functional significance of the hyporheic zone in streams and rivers. *Ann. Rev. Ecol. Syst.* **29**: 59–81 https://doi.org/10.1146/annurev.ecolsys.29.1.59.

Bradford JH, Clement WP, Barrash W. 2009. Estimating porosity with ground-penetrating radar reflection tomography: A controlled 3-D experiment at the Boise Hydrogeophysical Research Site. *Water Resources Research* **46**: W00D26. https://doi.org/10.1029/2008WR006960.

Brardinoni F, Hassan MA. 2007. Glacially induced organization of channel-reach morphology in mountain streams. *Journal of Geophysical Research: Earth Surface* **112**: 1–18. https://doi.org/10.1029/2006JF000741.

Bridge J. 2003. *Rivers and Floodplains: Forms, Processes, and Sedimentary Record*. Blackwell Publishing USA: Cornwall, UK.

Bridge J. 2009. Advances in fluvial sedimentology using GPR. In *Ground Penetrating Radar Theory and Applications*, Jol HM (ed). Elsevier Science Location: Great Britain; 323–359.

Bridge JS, Alexander J, Collier Richard EL, Gawthorpe RL, Jarvis J. 1995. Ground penetrating radar and coring used to study the large scale structure of point bar deposits in three dimensions. *Sedimentology* **42**: 839–852. https://doi.org/10.1111/j.1365-3091.1995.tb00413.x.

Brunke M, Gonser T. 1997. The ecological significance of exchange processes between rivers and groundwater. *Freshwater Biology* **37**: 1–33.

Buffington JM, Tonina D. 2009. Hyporheic exchange in mountain rivers II: Effects of channel morphology on mechanics, scales, and rates of exchange. *Geography Compass* **3**: 1038–1062 https://doi.org/10.1111/j.1749-8198.2009.00225.x.

Butler JJ, Healey JM. 1998. Relationships between pumping-test and slug-test parameters: Scale effect or artifact? *Groundwater* **36**: 305–312.

Dagan G. 1988. Time-dependent macrodispersion for solute transport in anisotropic heterogeneous aquifers. *Water Resources Research* **24**: 1491–1500 https://doi.org/10.1029/WR024i009p01491.

Davis JL, Annan AP. 1989. Ground-penetrating radar for high-resolution mapping of soil and rock stratigraphy. *Gephysical Prospecting* **37**: 531–551. https://doi.org/10.1111/j.1365-2478.1989.tb02221.x.

Egger G, Politt E, Lautsch E, Benjankar R, Gill K, Rood S. 2015. Floodplain Forest Succession Phases Reveal Fluvial Processes: A Hydrogeomorphic Model for Temperate Riparian Woodlands Assessment. *Journal of environmental management* **161**: 72–82.

Ekes C, Hickin EJ. 2001. Ground penetrating radar faces of the paraglacial Cheekye Fan, southwestern British Columbia, Canada. *Sedimentary Geology* **143**: 199–217.

EPA. 2017. Analysis of the transport and fate of materials released from the Gold King Mine in the Animas and San Juan Rivers. Washington, DC. USA [online] Available from: https://www.epa.gov/goldkingmine/fate-transport-analysis#additionalmaterials

Findlay S. 1995. Importance of surface-subsurface exchange in stream ecosystems: The hyporheic zone. *Limnology and Oceanography* **40**: 159–164.

Fogg, G. E., Carle, S. F., & Green, C. 2000. Connected network paradigm for the alluvial aquifer system. Theory, Mondeling and Field Investigation in Hydrology: A Special Volume in Honor of Shlomo P. Neuman's 60th Birthday, Special Publication of the Geological Society of America, 25–42.

Freeman MC, Pringle CM, Jackson CR. 2007. Hydrologic connectivity and the contribution of stream headwaters to ecological integrity at regional scales. *Journal of the American Water Resources Association* **43**: 5–14 https://doi.org/10.1111/j.1752-1688.2007.00002.x.

Fuchs JW, Fox GA, Storm DE, Penn CJ, Brown GO. 2009. Subsurface Transport of Phosphorus in Riparian Floodplains: Influence of Preferential Flow Paths. *Journal of Environment Quality* **38**: 473. https://doi.org/10.2134/jeq2008.0201.

Gaskill DL, Mutschler FE, Kramer JH, Thomas JA, Zahony SG. 1991. *Geologic Map of the Gothic Quadrangle*. Gunnison County: Colorado.

Gelhar LW, Axness CL. 1983. Three-dimensional stochastic analysis of macrodispersion in aquifers. *Water Resources Research* **19**: 161–180.

Gomez-Velez JD, Harvey JW. 2014. A hydrogeomorphic river network model predicts where and why hyporheic exchange is important in

© 2019 John Wiley & Sons, Ltd.

large basins. *Geophysical Research Letters*: 1–10. https://doi.org/10.1002/2014GL061099.Received.

Gomez-Velez JD, Harvey JW, Cardenas MB, Kiel B. 2015. Denitrification in the Mississippi River network controlled by flow through river bedforms. *Nature Geoscience* **8**: 941–945. https://doi.org/10.1038/ngeo2567.

Greco SE, Fremier AK, Larsen EW, Plant RE. 2007. A tool for tracking floodplain age land surface patterns on a large meandering river with applications for ecological planning and restoration design. *Landscape and Urban Planning* **81**: 354–373. https://doi.org/10.1016/j.landurbplan.2007.01.002.

Greene SL, Knox JC. 2014. Coupling legacy geomorphic surface facies to riparian vegetation: Assessing red cedar invasion along the Missouri River downstream of Gavins Point dam, South Dakota. *Geomorphology* **204**: 277–286. https://doi.org/10.1016/j.geomorph.2013.08.012.

Güneralp Í, Rhoads BL. 2011. Influence of floodplain erosional heterogeneity on planform complexity of meandering rivers. *Geophysical Research Letters* **38**: 2–7 https://doi.org/10.1029/2011GL048134.

Harte J, Shaw R. 1995. Shifting dominance within a montane vegetation community: Results of a climate-warming experiment. *Science* **267**: 876.

Harvey JW, Fuller CC. 1998. Effect of enhanced manganese oxidation in the hyporheic zone on basin-scale geochemical mass balance. *Water Resources Research* **34**: 623–636 https://doi.org/10.1029/97WR03606.

Harvey JW, Gooseff MN. 2015. River corridor science: Hydrologic exchange and ecological consequences from bedforms to basins. *Water Resources Research*: 1–30 https://doi.org/10.1002/2015WR017617.

Heeren DM, Fox GA, Miller RB, Storm DE, Fox AK, Penn CJ, Halihan T, Mittelstet AR. 2011. Stage-dependent transient storage of phosphorus in alluvial floodplains. *Hydrological Processes* **25**: 3230–3243. https://doi.org/10.1002/hyp.8054.

Heeren DM, Miller R, Fox GA, Storm DE, Halihan T, Penn CJ. 2010. Preferential flow effects on subsurface contaminant transport in alluvial floodplains. *Transactions of the ASABE* **53**: 127–136.

Hooke JM. 2007. Spatial variability, mechanisms and propagation of change in an active meandering river. *Geomorphology* **84**: 277–296. https://doi.org/10.1016/j.geomorph.2006.06.005.

Howard AD. 1992. *Modelling channel migration and floodplain sedimentation in meandering streams*. Lowland Floodplain Rivers: Geomorphological Perspectives; 1–41.

Howard AD. 1996. Modelling Channel Evolution and Floodplain Morphology. *Floodplain Processes*: 15–62.

Hvorslev MJ. 1951. Time lag and soil permeability in ground-water observations. Waterways Experiment Station, U.S. Army Corps of Engineers 36: 50.

Johnson A. 1963. *Specific Yields: Compilation of specific yields for various materials*: Denver, CO.

Jol HM, Smith DG. 1991. Ground penetrating radar of northern lacustrine deltas. *Canadiaon Journal of Earth Sciences* **28**: 1939–1947.

Jones KL, Poole GC, Woessner WW, Vitale MV, Boer BR, O'daniel SJ, Geffen BA. 2008. Geomorphology, hydrology, and aquatic vegetation drive seasonal hyporheic flow patterns across a gravel-dominated floodplain. *Hydrological Processes: An International Journal* **22**: 2105–2113.

Kiel BA, Cardenas MB. 2014. Lateral hyporheic exchange throughout the Mississippi River network. *Nature Geoscience* **7**: 413–417 https://doi.org/10.1038/NGEO2157.

Koltermann E, Gorelick SM. 1996. Heterogeneity in Sedimentary Deposits: A Review of Structure-Imitating, Process-Imitating, and descriptive approaches. *Water Resources Research* **32**: 2617–2658 https://doi.org/10.1029/96WR00025.

Kostic B, Aigner T. 2007. Sedimentary architecture and 3-D ground-penetrating radar analysis of gravelly meandering river deposits (Neckar Valley, SW Germany). *Sedimentology* **54**: 789–808.

Krause S, Tecklenburg C, Munz M, Naden E. 2013. Streambed nitrogen cycling beyond the hyporheic zone: Flow controls on horizontal patterns and depth distribution of nitrate and dissolved oxygen in the upwelling groundwater of a lowland river. *Journal of Geophysical Research: Biogeosciences* **118**: 54–67.

Larsen LG, Choi J, Nungesser MK, Harvey JW. 2012. Directional connectivity in hydrology and ecology. *Ecological Applications* **22**: 2204–2220.

Livers B, Wohl E. 2015. An evaluation of stream characteristics in glacial versus fluvial process domains in the Colorado Front Range. *Geomorphology* **231**: 72–82. https://doi.org/10.1016/j.geomorph.2014.12.003.

McFeeters SK. 1996. The use of the Normalized Difference Water Index (NDWI) in the delineation of open water features. *International journal of remote sensing* **17**: 1425–1432.

Miall AD. 2014. The Facies and Architecture of Fluvial Systems, Chapter 2. In *Fluvial Depositional Systems*. Springer Geology; 9–68 https://doi.org/10.1007/978-3-319-00666-6.

Miall AD. 1996. *The Geology of Fluvial Deposits: Sedimentary Facies, Basin Analysis, and Petroleum Geology*. Springer Verlag: Berlin.

Miller RB, Heeren DM, Fox GA, Halihan T, Storm DE, Mittelstet AR. 2014. The hydraulic conductivity structure of gravel-dominated vadose zones within alluvial floodplains. *Journal of Hydrology* **513**: 229–240.

Motta D, Abad JD, Langendoen EJ, García MH. 2012. The effects of floodplain soil heterogeneity on meander planform shape. *Water Resources Research* **48**: 1–17 https://doi.org/10.1029/2011WR011601.

Mulligan A, Uchupi E. 2003. New interpretation of glacial history of Cape Cod may have important implications for groundwater contaminant transport. *Eos* **84**: 3–6.

Notebaert B, Verstraeten G, Govers G, Poesen J. 2009. Qualitative and quantitative applications of LiDAR imagery in fluvial geomorphology. *Earth Surface Processes and Landforms* **34**: 217–231.

Pai H, Malenda H, Briggs M, Singha K, González-Pinzón R, Gooseff M, Tyler SW, the AirCTEMPS Team. 2017. Potential for small unmanned aerial systems applications for identifying groundwater-surface water exchange characteristics in a meandering river reach. *Geophysical Research Letters*: 44. https://doi.org/10.1002/2017GL075836.

Poole GC, Stanford JA, Frissell CA, Running SW. 2002. Three-dimensional mapping of geomorphic controls on flood-plain hydrology and connectivity from aerial photos. *Geomorphology* **48**: 329–347 https://doi.org/10.1016/S0169-555X(02)00078-8.

Poole GC, Stanford JA, Running SW, Frissell CA. 2006. Multiscale geomorphic drivers of groundwater flow paths: subsurface hydrologic dynamics and hyporheic habitat diversity. *Journal of the North American Benthological Society* **25**: 288–303 https://doi.org/10.1899/0887-3593(2006)25[288:MGDOGF]2.0.CO;2.

Pringle C. 2003. What is hydrologic connectivity and why is it ecologically important? *Hydrological Processes* **17**: 2685–2689 https://doi.org/10.1002/hyp.5145.

Revelli R, Boano F, Camporeale C, Ridolfi L. 2008. Intra-meander hyporheic flow in alluvial rivers. *Water Resources Research* **44**: 1–10. https://doi.org/10.1029/2008WR007081.

Rosgen DL. 1996. *Applied River Morphology*. Pagosa Springs, Colorado: Wildland Hydrology.

Rovey CWI, Cherkauer DS. 1995. Scale dependency of hydraulic conductivity measurements. *Groundwater* **33**: 769–780.

Rovey CWI, Niemann WL. 2001. Wellskins and slug tests: Where's the bias? *Journal of Hydrology* **243**: 120–132.

Savoy H, Kalbacher T, Dietrich P, Rubin Y. 2017. Geological heterogeneity: Goal-oriented simplification of structure and characterization needs. *Advances in Water Resources* **109**: 1–13 https://doi.org/10.1016/j.advwatres.2017.08.017.

Skelly RL, Bristow CS, Etheridge FG. 2003. Architecture of channel-belt deposits in an aggrading shallow sandbed braided river: The lower Niobrara river, northeast Nebraska. *Sedimentary Geology* **158**: 249–270.

Słowik M. 2016. The influence of meander bend evolution on the formation of multiple cutoffs: Findings inferred from floodplain architecture and bend geometry. *Earth Surface Processes and Landforms* **41**: 626–641. https://doi.org/10.1002/esp.3851.

Stollenwerk KG, Grove DB. 1985. Adsorption and desorption of hexavalent chromium in an alluvial aquifer near Telluride, Colorado. *Journal of Environment Quality* **14**: 150–155.

Stone MC, Byrne CF, Morrison RR. 2017. Evaluating the impacts of hydrologic and geomorphic alterations on floodplain connectivity. *Ecohydrology* **10**: e1833.

© 2019 John Wiley & Sons, Ltd.

Thein SJ. 1979. A flow diagram for teaching texture by feel analysis. *Journal of Agronomic Education* **8**: 54–55.

Tockner K, Pennetzdorfer D, Reiner N, Schiemer F, Ward JV. 1999. Hydrological connectivity, and the exchange of organic matter and nutrients in a dynamic river–floodplain system (Danube, Austria). *Freshwater Biology* **41**: 521–535.

Todd DK. 1980. *Groundwater Hydrology*, 2nd edn. Wiley.

Tonina D, Buffington JM. 2007. Hyporheic exchange in gravel bed rivers with pool-riffle morphology: Laboratory experiments and three-dimensional modeling. *Water Resources Research* **43**(1): 1–16 https://doi.org/10.1029/2005WR004328.

Toonen WHJ, Kleinhans MG, Cohen KM. 2012. Sedimentary architecture of abandoned channel fills. *Earth Surface Processes and Landforms* **37**: 459–472. https://doi.org/10.1002/esp.3189.

Vandenberghe J, Van Overmeeren RA. 1999. Ground penetrating radar images of selected fluvial deposits in the Netherlands. *Sedimentary Geology* **128**: 245–270. https://doi.org/10.1016/S0037-0738(99)00072-X.

Van Den Berg EH, De Vries JJ. 2003. Influence of grain fabric and lamination on the anisotropy of hydraulic conductivity in unconsolidated dune sands. *Journal of Hydrology* **283**: 244–266 https://doi.org/10.1016/S0022-1694(03)00272-5.

Van Dijk WM, Van de Lageweg WI, Kleinhans MG. 2013. Formation of a cohesive floodplain in a dynamic experimental meandering river. *Earth Surface Processes and Landforms* **38**: 1550–1565. https://doi.org/10.1002/esp.3400.

Van Dijk WM, Van De Lageweg WI, Kleinhans MG. 2012. Experimental meandering river with chute cutoffs. *Journal of Geophysical Research: Earth Surface* **117**: 1–18. https://doi.org/10.1029/2011JF002314.

Van Dijk WM, Schuurman F, Van de Lageweg WI, Kleinhans MG. 2014. Bifurcation instability and chute cutoff development in meandering gravel-bed rivers. *Geomorphology* **213**: 277–291. https://doi.org/10.1016/j.geomorph.2014.01.018.

Van Overmeeren RA. 1998. Radar facies of unconsolidated sediments in The Netherlands: A radar stratigraphy interpretation method for hydrogeology. *Journal of Applied Geophysics* **40**: 1–18. https://doi.org/10.1016/S0926-9851(97)00033-5.

Winnick MJ, Carroll RWH, Williams KE, Maxwell RM, Dong W, Maher K. 2017. Water Resources Research. *Water Resources Research*. **53**: 2507–2523. https://doi.org/10.1002/2016WR019724.Received.

Wohl E. 2004. Limits of downstream hydraulic geometry. *Geology* **32**: 897–900. https://doi.org/10.1130/G20738.1.

Wondzell SM. 2006. Effect of morphology and discharge on hyporheic exchange flows in two small streams in the Cascade Mountains of Oregon, USA. *Hydrological Processes: An International Journal* **20**: 267–287.

Xie Y, Sha Z, Yu M. 2008. Remote sensing imagery in vegetation mapping: A review. *Journal of Plant Ecology* **1**: 9–23.

Zhang Y, Green CT, Fogg GE. 2013. The impact of medium architecture of alluvial settings on non-Fickian transport. *Advances in Water Resources* **54**: 78–99. https://doi.org/10.1016/j.advwatres.2013.01.004.

Supporting Information

Additional supporting information may be found online in the Supporting Information section at the end of the article.

Table S1: Processing Notes for GPR transects. Gain type, attenuation, start gain, maximum gain, and velocity are standard parameters related to GPR data processing. The prefixes "A", "D", and "SR" indicate Meander A, D, and the Straight Reach (near the 2007 cutoff), respectively. "PZ" indicates piezometer associated with each transect. Water levels, in meters, are depths to water below ground surface.

Table S2: Location and water level data measured at each piezometer and used in gradient calculations. Water level data are in meters above mean sea level.

Table S3: Summary table of water table gradients' magnitudes calculated using different three-point configurations at Meander A and Meander D. Bolded gradients are used for estimates in Table 4.

Figure S1: Radar facies described in the East River floodplain. Key features are highlighted in red. SI1a: former channel (SRL-2 in Figure 3); SI1b: lateral accretion structures (DL-1 in Figure 3), cut bank denoted in yellow; SI1c: point bar (SRL-1 in Figure 3); SI1d: heterogeneous gravels (AL-2 in Figure 3).

Figure S2: Non-annotated GPR transects collected at Meander A.

Figure S3: Stratigraphic interpretation of GPR transects along Meander A

Figure S4: Non-annotated GPR transects collected at Meander D.

Figure S5: Former channel locations as shown in historical images. The most recent channel configuration (2015) is plotted below all the other years in each panel for spatial reference. Elevation/NDVI mapped channels are in grey.

Figure S6: Channel reconstructions (1955-2015) based on historical photography (rainbow) and elevation/NDVI (grey). Note multiple historical cutoffs upstream and downstream of Meander D.

© 2019 John Wiley & Sons, Ltd.